


 Cite this: *RSC Adv.*, 2022, **12**, 25654

# Preparation, characterization, and performance of PES/GO woven mixed matrix nanocomposite forward osmosis membrane for water desalination†

 Mervat Nasr,<sup>1</sup> <sup>\*ab</sup> Nada Alfryyan,<sup>2</sup> Sahar S. Ali,<sup>1</sup> <sup>d</sup> Hanafy M. Abd El-Salam<sup>a</sup> and Mohamed Shaban<sup>1</sup> <sup>be</sup>

Mixed matrix woven forward osmosis (MMWFO) membranes made of polyethersulfone (PES)/graphene oxide nanosheets (GO NSs) were made by inserting varying wt% ratios of GO NSs (zero to 0.1 wt%) into the PES matrix. A coated woven fabric material was used to cast the membrane polymer solution. The physical characteristics and chemical structures of the produced PES/GO MMWFO membranes were studied, including contact angle, hydrophilicity, porosity, tortuosity, function groups, chemical and crystallographic structures, nanomorphologies, and surface roughness. The performance of the prepared PES/GO FO membranes for water desalination was evaluated in terms of pure water flux ( $J_w$ ), reverse salt flux ( $J_s$ ), and salt rejection (SR). The hydrophilicity and porosity of the FO membrane improved with the addition of GO NSs, as did water permeability due to the development of multiple skin-layer structures with greater GO NS loading. These GO NSs establish shortcut pathways for water molecules to move through, reducing support layer tortuosity by three times, lowering support layer structural features, and minimizing internal concentration polarization (ICP). The PES/0.01 wt% GO MMWFO membrane with a total casting thickness of 215  $\mu\text{m}$  and 1 M NaCl concentration had the best performance, with the highest  $J_w$  (114.7 LMH), lowest  $J_s$  (0.03 GMH), and lowest specific reverse solute flux ( $J_s/J_w = 0.00026 \text{ g L}^{-1}$ ), as well as a more favorable structural parameter ( $S = 149 \text{ }\mu\text{m}$ ). The performance of our optimized membrane is significantly better than that of the control woven commercial cellulose triacetate (CTA) FO membrane under optimal FO conditions. As the NaCl concentration increased from 0.6 to 2 M,  $J_w$  increased from 105 to 127 LMH which is much higher than the  $J_w$  of the commercial one (7.2 to 15 LMH). Our FO membranes have an SR of 99.2%@0.65 M NaCl, which is significantly greater than that of the CTA membrane.

 Received 21st June 2022  
 Accepted 13th August 2022

 DOI: 10.1039/d2ra03832c  
[rsc.li/rsc-advances](http://rsc.li/rsc-advances)

## 1 Introduction

Desalination is becoming an important part of dealing with global water scarcity issues. Although current desalination methods like thermal distillation, reverse osmosis (RO), and forward osmosis (FO) have made a significant contribution to the success of sea/brackish water desalination, additional research is required.<sup>1</sup> Artificial polymeric membrane technology

has received a lot of attention from both academia and industry.<sup>2,3</sup> Membrane technology's advantages over other operating technologies are based on the membrane selectivity separation idea, which may be carried out isothermally and with minimal energy usage.<sup>4,5</sup> Membrane processes are energy efficient, easy to run, scale up and down, and operate at room temperature, which prevents product change or deterioration.<sup>6-9</sup> A membrane is a semi-permeable barrier that facilitates the transfer of one or more compounds under a certain driving force, such as molecules, particles, gases, and/or a liquid mixture or solution.<sup>9-12</sup> Depending on the driving force of separation and the particle size of the separated species, the driving force across the membrane can be quantified as a difference in pressure, concentration, and voltage.<sup>13</sup> Forward osmosis (FO) is gaining popularity as a cost-effective alternative to traditional membrane technologies, notably reverse osmosis (RO), for brackish and seawater desalination, wastewater treatment, osmotic power production, and food processing.<sup>14-22</sup> The driving force in the FO process is naturally created by the osmotic pressure differences created by the more concentrated

<sup>a</sup>Chemistry Department, Faculty of Science, Beni-Suef University, Beni-Suef 62514, Egypt. E-mail: mohamed.fadel@science.bsu.edu.eg

<sup>b</sup>Nanophotonics and Applications (NPA) Lab, Physics Department, Faculty of Science, Beni-Suef University, Beni-Suef, 62514, Egypt

<sup>c</sup>Department of Physics, College of Sciences, Princess Nourah bint Abdulrahman University, P.O. Box 84428, Riyadh 11671, Saudi Arabia

<sup>d</sup>Chemical Engineering and Pilot-Plant Department, National Research Center, P.O. Box 12622, Dokki, Cairo, Egypt

<sup>e</sup>Department of Physics, Faculty of Science, Islamic University of Madinah, Al-Madinah Al-Munawarah, 42351, Saudi Arabia

† Electronic supplementary information (ESI) available. See <https://doi.org/10.1039/d2ra03832c>



draw solution (DS) on the permeate side of the membrane.<sup>23,24</sup> Furthermore, adopting a low working pressure in the FO process decreases fouling, lowers cleaning frequency, and perhaps improves membrane longevity.<sup>25–27</sup> As a result, FO is a superior technology to RO, as indicated by the significant growth in FO research papers in the recent 2–3 years. Recent research has concentrated on strategies to improve the characteristics of the FO membrane, particularly at the top active skin layer, due to the inherent benefits that the FO membrane gives in the water desalination process.<sup>26,28</sup> The FO process offers many benefits over standard RO processes, including lower energy consumption and a lesser inclination for clogging.<sup>29,30</sup> FO has also been investigated for the treatment of wastewater, anaerobic digestion, and shale gas drilling backflow fluid.<sup>16,31,32</sup> The FO process, however, presents a few important challenges being a relatively new technology that must be overcome. FO membranes must enhance their performance and economic viability. The FO membrane might be one of the most critical elements in its economic feasibility, given the FO process's very low water flow compared to other membrane processes such as RO. Dilutive internal concentration polarization (ICP), which must be addressed to enhance membrane performance, is the major cause of reduced water flow in the FO process.<sup>30,33,34</sup> On the active layer side of the FO membrane, external concentration polarization (ECP) occurs, while internal concentration polarization (ICP) occurs within the support layer, preventing draw solutes from diffusing into the substrate layer.<sup>35</sup> While the ECP can be reduced by adjusting hydrodynamic operating conditions such as crossflow velocity, the ICP cannot be reduced by adjusting hydrodynamic operating conditions alone. ICP can be reduced by enhancing the intrinsic features of the membrane support layer, such as porosity, pore size distribution, tortuosity, and thickness.<sup>36,37</sup> The structural parameter (*S* value) is commonly used to indirectly evaluate the degree of the ICP effect in the FO process as an indicative measure for membrane property.<sup>38</sup> Few studies have recently presented FO membranes with thin substrates of low *S* value, high porosity with macro-voids, and high wettability to reduce ICP and enhance water permeability.<sup>33,39</sup> The majority of efforts to construct FO membranes have focused on creating a very porous membrane substrate with finger-like macro-voids, which can be achieved by lowering the polymer concentration during the phase inversion process. Polymeric membranes are frequently employed because of their ease of manufacture, flexibility, toughness, and low cost. However, they have poor mechanical, chemical, and thermal resistance, as well as anti-fouling properties.<sup>40–42</sup> Their low anti-fouling efficacy was attributed to their hydrophobic nature. Membrane modification methods such as bulk modification, surface coating, and mixing have all been developed to improve membrane characteristics. An inorganic nanomaterial, such as carbon nanotubes (CNTs),<sup>43</sup> titanium oxide,<sup>44</sup> or zeolite,<sup>45</sup> can be used as a modifier to increase the polymeric membranes' selectivity, strength, antifouling, and permeability properties. Among suggested modifiers, the inclusion of GO NSs can improve the wettability, chemical stability, porosity, and anti-fouling performance of TFC FO membranes.<sup>46,47</sup> According to

our understanding, GO incorporation into PES substrate can boost membrane pore width, porosity, and hydrophilicity due to the abundance of hydrophilic functional groups on its surface, such as hydroxyl, epoxide, carbonyl, and carboxyl, which significantly can increase water permeability. A huge surface area and excellent mechanical qualities are also associated with GO. It has previously been used as a nanofiller to increase water permeability, anti-fouling, and chlorine resistance in membrane selective layer production.<sup>48–51</sup> Membranes made of polyether sulfone (PES) are frequently employed in water desalination and biomedical areas. With a high glass temperature, the PES membrane offers good thermal, mechanical, and oxidative properties. The hydrophobicity of the PES membrane, which acts as a separation barrier, might be seen as a drawback. Because of its simplicity, low cost, and large output, the phase inversion method is the most often used technique for PES-based membrane preparation. This process is also more practical than other ways of combining polymer matrices with various nanostructures to increase their performance. According to Shaban *et al.*, adding titanium nanotubes to PES increases membrane porosity and improves membrane performance.<sup>52</sup> This study used a woven fabric as backing support to investigate the integration of GO NSs into PES FO membrane properties and performance. The effects of various GO NSs weight-percentage ratios on morphology, total porosity, contact angle, water flux, reverse salt flux, and salt rejection were studied. The performance of the membrane filtering system was assessed in the FO mode, with distilled water as the feed solution and 1 M NaCl as the draw solution, with the active layer facing the feed solution (AL-FS). The originality of this research lies in the preparation and optimization of MMWGO/PES membranes by combining PES with ultrathin multi-layer nano sheet GO at different concentrations, which results in a multi-thin layer of honey comp pore structure that increases water transportability (higher flux) and filterability. Furthermore, using a woven fabric with a sizable open area and an evenly distributed, compacted nano sheet GO layer will enhance the functionality and antifouling properties of the FO membrane. Additionally, membranes made with ultrathin multilayer nano GO that embed and coat, respectively, the top and bottom surfaces of the woven fabric boost water flux and minimize reverse salt flux.

## 2 Experimental details

### 2.1 Materials

Polyethersulfone (PES ultrason E6020P,  $M_w = 58\,000\text{ g mol}^{-1}$ ) was supplied by BASF Company, Germany. *N,N*-Dimethylformamide (DMF) (CAS no. 68-12-2), polyethylene glycol (PEG),  $H_2SO_4$ , and  $H_3PO_4$  were purchased from Sigma-Aldrich, Germany. Graphite was purchased from VEB Laborchemie Apolda, Germany.  $H_2O_2$  and  $KMnO_4$  were purchased from Adwic Company, Egypt. The commercial CTA FO membranes supplied by Hydration Technology Innovation (HTI, Albany, USA) which is denoted as HTI-CTA was used for comparison.

**2.1.1 Woven support.** Using woven support with a smooth surface and regular fibre distribution in a woven structure can



result in a high permeate flux (*i.e.*, increasing fabric open area) due to an increase in membrane permeability. In general, any open mesh fabric can be used to support a membrane.<sup>52–54</sup> During the casting process, the support fabric is completely covered by the membrane material. The mechanical properties of woven fabric support are studied and presented in Table S1 (ESI Data†). The tensile strength (31.22 N cm<sup>−2</sup>) and elongation (44.2 mm) of the woven support were measured using the mechanical testing system model H5KS Tinius Olsen. The contact angle was also measured to be 41°. The fibre diameter and woven fabric thickness were ~11.6 and 115 μm, respectively.

**2.1.2. Permeability test.** The permeability test was carried out on the fabric support using distilled water. The test was performed using a filtration lab unit with a diameter of 5 cm. This unit has three openings, one for feeding, the second for the reject, and the third for permeating. The reject side was closed to perform a pressure on the sample. The woven fabric permeability was ~1254 (LMH bar).

## 2.2 Methods

**2.2.1 Fabrication of GO NSs by modified Hummer's method.** GO NSs have been fabricated by using a modified Hummer's method. In brief, 1 g of graphite powder was added to a combination of 120 mL H<sub>2</sub>SO<sub>4</sub> and 14 mL H<sub>3</sub>PO<sub>4</sub>. Then, 6 g of KMnO<sub>4</sub> was added slowly over 1 hour in an ice bath and stirred at the rate (300 rpm). After that, the solution was kept at 50 °C for 24 hours. In the next step, 800 mL of deionized water (DW) and 10 mL of hydrogen peroxide (H<sub>2</sub>O<sub>2</sub>) were added drop by drop alternately to graphite suspended solution in an ice bath, to minimize the KMnO<sub>4</sub> residue, and generate a large number of air bubbles. Finally, the color of the solution changed to a radish yellow color. The obtained precipitate was collected and washed with DW and methanol several times till the solution become neutral (pH 7), then dried at 60 °C to produce GO powder.

**2.2.2 Characterization of GO NSs.** The prepared GO NSs were characterized using various analytical techniques. X-ray diffraction technique (XRD; PANalytical X'Pert Pro, Holland) was used to investigate the structural properties of prepared GO. Morphological analyses were examined by using a scanning electron microscope (SEM; FEI Quanta 200, USA), and a scanning transmission electron microscope (STEM; ZEISS SUPRA 55 VP, Gemini Column). An energy-dispersive X-ray unit (EDX; Oxford Link ISIS 300, Concord, MA, USA) was used to study the chemical ratio composition of the resultant GO. The purity of the GO powder was checked by using a Raman Spectrometer (Thermo Fisher Scientific, model DXR3xi, USA) with a 532 nm laser.

**2.2.3. Fabrication of PES/GO MMW FO membranes.** The phase inversion method was used for preparing PES/GO MMW membranes and is ready to be used in FO application.<sup>55–57</sup> Casting PES solutions were prepared by dissolving different chemical ratios (20 wt% PES, 1 wt% PEG, and GO NSs with different weight ratios) in DMF solvent with different weight ratios as listed in Table 1 according to the following steps:

**Table 1** Composition of PES/GO MMW FO membranes prepared with different GO NSs wt%

Membrane ID	PES (wt%)	DMF (wt%)	GO NSs (wt%)	PEG (wt%)
Bare PES	20	79	0	1
SG1	20	78.996	0.004	1
SG2	20	78.992	0.008	1
SG3	20	78.99	0.01	1
SG4	20	78.96	0.04	1
SG5	20	78.92	0.08	1
SG6	20	78.9	0.1	1

firstly, different weight ratios of GO NSs and 1 wt% PEG were dispersed in different weight ratios of DMF solvent by using an ultrasonic bath device for 4 h at room temperature to obtain a uniform dispersion of GO NSs in casting solution. Secondly, the 20 wt% of PES has been added to the prepared casting solution under a mechanical stirrer for 2 h at room temperature to obtain homogeneity. Then, the casting solution was left for 24 h to remove any air bubbles and be ready for casting to get the membrane. Finally, the casting solution was cast on a coated woven fabric as a support material with a different total casting thickness (215 and 265 μm) using a casting knife followed by immersed in the water immediately as a non-solvent bath. The fabricated membranes are left in fresh DW tanks for 24 hours until the phase inversion process is complete by ensuring after which membrane has separated from the glass plate. The membrane was skinned and washed with DW to remove any residual solvent in the membrane. Finally, the prepared membrane was stored in fresh DW and used for further characterization.

### 2.2.4. PES/GO MMW FO membrane characterization

**2.2.4.1 Morphology and contact angle.** SEM images of membrane samples were obtained by a field-emission scanning electron microscope (FESEM, ZEISS SUPRA 55 VP, Gemini Column). Membrane samples were dried in an oven at the temperature of 30 °C before the test. Cutting the membrane with one sharp blow was done for cross-section SEM imaging. Surface roughness utilizing Image j software (v5.0.3) for analysis. Fourier transform infrared spectroscopy (ATR-FTIR, VERTEX 70, Bruker) in the range of 600–4000 cm<sup>−1</sup> was used to recognize the functional groups of the membrane. The contact angle plays an important role to describe the hydrophobicity of membrane and membrane fouling. The contact angle of the PES/GO MMW was measured by the sessile drop method, and measurements were carried out at least three times, and the average values were taken to minimize the error. The physical parameters such as membrane contact angle, water uptake, porosity, tortuosity, and structure parameter were determined for PES and PES/GO MMW FO membranes.

**2.2.4.2 Water uptake rate.** The weight change after hydration was used to measure the water uptake rate and porosity of modified PES/GO MMW FO membranes. The membrane was initially soaked for 24 hours in DW at room temperature. After cleaning the surface with filter paper, the membrane was promptly weighed to estimate the weight of the wetted



membrane ( $W_w$ ). After that, the wet membranes were dried for 24 hours in an air-circulating oven at 80 °C, and then the dried membranes were weighed ( $W_d$ ).

The following equation was used to calculate the percentage of water uptake:<sup>58</sup>

$$\text{Water uptake}(\%) = \frac{(W_w - W_d)}{W_d} \times 100 \quad (1)$$

**2.2.4.3 Porosity ( $P$ ).** The membrane porosity of membranes was calculated using the following equation:<sup>59</sup>

$$\text{Porosity}(\%) = \frac{(W_w - W_d)}{V} \times 100 \quad (2)$$

$W_w$  and  $W_d$  are the weights of wet and dry membranes (g), respectively; and  $P$  is the membrane porosity.  $V = A \times t$ , where  $A$  is the membrane surface area (cm<sup>2</sup>), and  $t$  is the membrane thickness (cm).

**2.2.4.4 Tortuosity ( $\tau$ ) and structure parameter ( $S$ ).** Membrane tortuosity ( $\tau$ ) can calculate using eqn (3) by the porosity of the membrane:<sup>60</sup>

$$\tau = \frac{(2 - \varepsilon)^2}{\varepsilon} \quad (3)$$

Membrane structural parameter ( $S$ ) is one of the critical properties of any osmotic membranes and is given by the following relationship that depends on the support layer thickness ( $t$ ) and tortuosity ( $\tau$ ) and its porosity ( $\varepsilon$ ).<sup>61</sup>

$$S = \frac{t \cdot \tau}{\varepsilon} \quad (4)$$

### 2.3 PES/GO MMW FO membrane performance

The performance of the fabricated PES/GO MMW membrane was carried out using a bench-scale FO setup.<sup>62</sup> A membrane with a surface area of 56 cm<sup>2</sup> was employed for the testing, which was done in the FO mode with the shiny face (active layer) facing feed solution (DW) and the other layer facing 1 M NaCl solution as draw solution, respectively. All FO testing experiment was applied at a fixed crossflow rate of 0.857 L min<sup>-1</sup> and room temperature. The FO membrane performance is represented as, water flux ( $J_w$ , LMH), reverse salt flux (RSF) ( $J_s$ , GMH), specific reverse salt flux (SRSF), ( $J_s/J_w$ , g L<sup>-1</sup>), and rejection ( $R\%$ ) was estimated as follows:

$$\text{The water flux} (J_w) = \frac{\Delta V}{A \cdot \Delta t} \quad (5)$$

where  $\Delta V$  (L) is the volume of water transported through the forward osmosis process within the interval time of  $\Delta t$  (h) and membrane effective area  $A$  (m<sup>2</sup>).

$$\text{The reverse salt flux} (J_s) = \frac{C_t V_t - C_0 V_0}{A t} \quad (6)$$

where  $C_t$  and  $C_0$  (mol L<sup>-1</sup>) are the final and initial salt concentrations in the feed solution, respectively. Also,  $V_t$  and  $V_0$

(L) represent the final and initial volume of the feed solution (FS), respectively.

**2.3.1 Salt rejection measurements.** A dead-end cell was used to measure salt rejection. The following approach was used to obtain the measurements:

1-The membrane was sliced into a 5 cm disc and placed in the test cell on a porous stainless-steel support.

2-The cell was filled with a 2000 mg L<sup>-1</sup> NaCl solution as the feed solution.

3-At three bars of pressure were adjusted.

4-To achieve a constant liquid flow rate, the membrane was fixed for 10 to 15 minutes.

5-In a measuring cylinder, the permeate solution was collected.

6-A conductivity meter (Janeway 2 s to 200 mS) was used to test the feed and permeate conductivities.

$$\text{Specific reverse salt flux (SRSF)} = \frac{J_s}{J_w} \quad (7)$$

$$\text{The salt rejection (SR)} = \left( 1 - \frac{C_p}{C_f} \right) \times 100\% \quad (8)$$

where  $R\%$  represents salt rejection,  $C_p$  represents permeate concentration, and  $C_f$  represents feed concentration.<sup>63</sup>

**2.3.2. Effect of total casting height.** The effect of total casting height of 215 μm and 265 μm on PES/GO MMWFO membrane performance at different GO NSs wt% of zero to 0.04 wt% and using PES as the main polymer of 20% and PEG of 1% as pore-forming using FO testing cell in FO mode where the shiny phase faced feed solution (distilled water) and another side is faced (NaCl of 1 M).

**2.3.3. Effect of GO concentrations on PES/GO MMW FO membrane performance.** The effect of different GO NSs wt% ratio from zero to 0.1 wt% on the PES/GO MMW membrane performance is investigated at PES of 20% and PEG of 1% as pore-forming at a total casting height of 215 μm using FO testing cell in FO mode where the shiny phase faced feed solution (distilled water) and the anther side is faced (NaCl of 1 M).

**2.3.4. Effect of time on PES/GO MMW FO membrane performance.** The effect of testing time on PES/GO MMW membrane performance at a total casting height of 215 μm and 0.01 wt% of GO NSs using PES as the main polymer of 20% and PEG of 1% as pore-forming. The membrane performance was carried out using an FO testing cell (sterile tech) in FO mode where the shiny phase faced feed solution (distilled water) and another side faced (NaCl of 1 M).

**2.3.5 Effect of different DS concentrations on (SG3) PES/GO MMW FO blend membrane.** The FO performance of the newly fabricated PES/GO MMW membrane was investigated at the optimum condition (total casting height of 215 μm) and 0.01 wt% of GO NSs using PES as the main polymer of 20% and PEG of 1% as pore-forming using NaCl solutions of different concentrations (0.6, 1, 1.5, and 2 M) as a draw solution and another side feed solution (distilled water).

**2.3.6 Comparison between PES/GO MMW FO blend membrane (SG3) and commercial woven FO CTA membrane.**



To evaluate the performance of the PES/GO MMW membrane (SG3), we carried out a comparison between the PES/GO MMW membrane (SG3) and commercial woven CTA membrane in FO mode using distilled water as a feed solution and NaCl of (0.6, 1, 1.5 and 2 M) solution at as draw solution.

### 3. Results and discussion

#### 3.1 Characterization of GO NSs prepared

**3.1.1 XRD of GO NSs.** Fig. 1 illustrates the XRD charts, EDX, and SEM images of GO nanomaterial. From the XRD spectrum in Fig. 1(A), the GO NSs show a diffraction pattern of the tetragonal GO crystalline phase. There are four characteristic peaks for the tetragonal GO phase with miller indices (001), (220), (221), and (322) located at  $2\theta$ -positions of  $10.5^\circ$ ,  $21^\circ$ ,  $26.7^\circ$ , and  $42.3^\circ$ ; based on a standard JCPDS card no. 96-590-0025.<sup>64</sup> In addition, the XRD chart does not detect any additional impurity phases for GO compounds. This implies the creation of pure

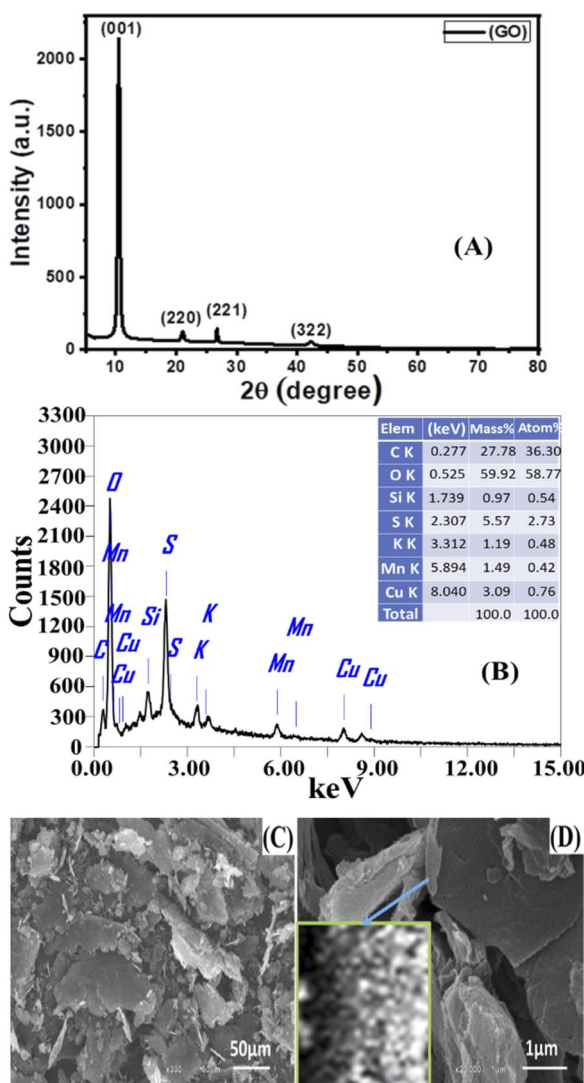


Fig. 1 (A) XRD chart, (B) EDX spectrum, and (C and D) SEM images of GO NSs.

crystalline and ordered structure GO nanosheets by modified Hummer's method.

The crystallite size ( $D$ ) of GO was estimated using the full width at half the maximum of the peaks ( $\beta$ ) from XRD data using Scherrer's formula:<sup>65,66</sup>

$$D = \frac{0.94 \lambda}{\beta \cos \theta} \quad (9)$$

Where  $\theta$  and  $\lambda$  are Bragg's angle and X-ray wavelength, respectively. From the calculation, the average GO crystallite size is nearly 23.6 nm.

Texture coefficient is an important parameter to identify preferential orientations for the growth of the crystallites. So, the effect of preparation conditions on the orientation of the GO was investigated by calculating the texture coefficient  $T_c(hkl)$  using the following equation:

$$T_c(hkl) = \frac{I(hkl)/I_0(hkl)}{\frac{1}{N} \left[ \sum \frac{I(hkl)}{I_0(hkl)} \right]} \quad (10)$$

where  $T_c(hkl)$  is the texture coefficient of the diffraction peaks,  $I$  is the measured intensity,  $I_0$  is the standard intensity obtained from the GO card (JCPDS) and  $N$  is the number of diffraction peaks. Fig. 1(A) shows a sharp peak and the highest intensity with miller indices (001) located at  $2\theta = 10.2^\circ$ , which is the preferred orientation for the growth of GO crystallites with a  $T_c$  value of 3.66, according to our  $T_c$  calculations. This finding around the (001) peak demonstrates that graphite (G) has been completely converted to graphene oxide (GO).<sup>67</sup> The (220) and (221) orientations have  $T_c$  values of 0.11 and 0.18, respectively.

**3.1.2 EDX for GO NSs.** The energy dispersive X-ray (EDX) method is usually used to identify the chemical composition and the quantitative ratios of the compositional elements. The EDX of GO NSs was performed at an applied voltage of 15 kV. Fig. 1(B) displays the EDX spectrum for GO NSs manufactured by the modified Hummer's method. The inset table gives the quantitative analysis of the chemical composition of the GO NSs. According to the inset table, there is one peak for O located at 0.525 keV and another major peak related to C at 0.277 keV. The high atomic intensity of C and O (36.3% and 58.77%) is due to the graphene oxide structure, which consists of carbon-oxygen atom bonds, suggesting that GO NSs were properly synthesized. These findings are consistent with XRD data, Fig. 1(A). However, there are other minor elements such as silicon (Si), sulfur (S), manganese (Mn), potassium (K), and copper (Cu). The main cause for the presence of S, K, and Mn is due to  $H_2SO_4$  and  $KMnO_4$  being used as oxidizing agents during GO preparation. The Si and Cu appear probably due to the chamber effect of SEM-EDX. It is not due to the content of graphene oxide.<sup>64</sup>

**3.1.3 SEM and TEM analysis of GO NSs.** The surface morphology of GO was examined using the SEM images in Fig. 1(C and D). The top morphology of GO is shown in Fig. 1(C and D) as a homogenous layered structure formed of a random distribution of fractured GO nanosheets (sheet-like structure) with a slight wrinkle. R. Siburian *et al.* got similar morphologies when they used Hummers' method to prepare the GO under the same conditions.<sup>67</sup> In addition, Fig. 1(D) includes a high



magnification SEM inset demonstrating that the GO nanosheet is made up of a nano/mesoporous-like structure.

A typical transmission electron microscope (TEM) examination for synthesized GO is shown in Fig. 2(A). The TEM revealed that the GO has a stacked sheet structure with a wrinkled edge that is a few nanometers in size. Moreover, during the oxidation process, a symmetrical shape (mesoporous structure) with a cracked structure appeared in Fig. 2(A). In addition, we note that GO is multi-folded sheets with a definite surface area. This may be attributed to van der Waals's interaction between every two adjacent sheets of GO and the agglomeration of GO sheets during the drying process.<sup>68</sup>

**3.1.4 Raman spectroscopy.** The Raman spectrum of GO NSs is shown in Fig. 2(B). The 532 nm wavelength of the exciting laser beam in Raman spectroscopy for the examination of GO NSs yielded the coordinates stated. It's a useful non-destructive method to identify the features of carbon-based materials.<sup>69</sup> The Raman spectrum reveals two peaks in GO NSs: the D and G bands, which are situated at 1360 and 1590 cm<sup>-1</sup>, respectively. The ratio value between the intensities of D and G bands (ID/IG) determines the degree of structural disorder. The D band in the Raman spectrum is linked with the conversion of sp<sup>2</sup> hybridized carbon to sp<sup>3</sup> hybridized carbon, while the G band is connected with the in-plane bond-stretching motion of the pair of C sp<sup>2</sup> atoms. As a result, GO may act as a monolayer as well as a multilayer. Because the water was eliminated during drying, the multilayer appeared owing to the stacking mode of graphene oxide in dried powder.<sup>70</sup>

### 3.2. PES/GO MMW FO membranes characterization

#### 3.2.1. FTIR analysis and function groups of PES/GO MMW FO membranes.

After the PES/GO MMW membranes were

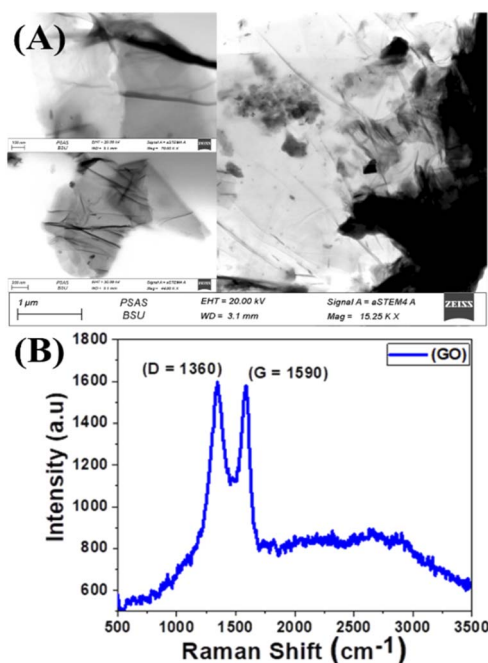


Fig. 2 (A) TEM images and (B) Raman spectrum of GO NSs.

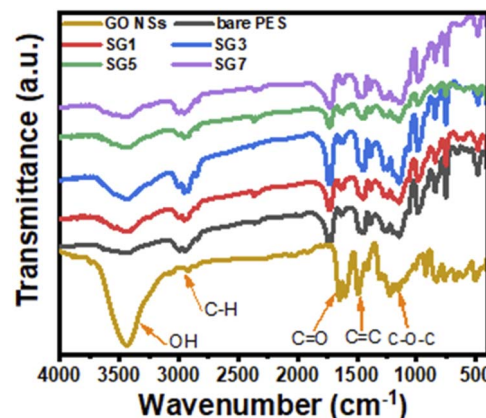


Fig. 3 FTIR spectra of bare PES and PES/GO MMW FO membranes with different GO NSs wt% ratios.

completely dried at room temperature, the FTIR analysis was performed. Fig. 3 shows FTIR spectra for fabricated bare PES membrane and the GO NSs-incorporated MMW membranes with different weight ratios. FTIR analysis was used to detect the chemical compositions and the functional groups of membranes due to the incorporation of GO NSs. Because of the hydroxyl functional groups (O-H) at GO NSs, the hydrophilicity of the membrane surface is expected to increase. GO is a hydrophilic compound with numerous functional groups, including hydroxyl (O-H = 3500 cm<sup>-1</sup>), carbonyl (C=O), and others, as shown from the GO FT-IR spectrum. This agrees with the information provided by Yu *et al.*<sup>71</sup> The considerable amounts of oxygen-containing functional groups, including carboxyl, hydroxyl, and carbonyl, that are present on GO and give it its hydrophilic qualities are caused by oxidation. As a result, adding GO to PES in different ratios boosts the concentration of hydroxyl groups until it reaches an optimal level, which enhances the hydrophilicity of the membrane. From Fig. 3, as the GO wt% ratio increases, the peak intensity of hydroxyl groups increases and is located at 3100–3600 cm<sup>-1</sup>. There are other characteristic peaks related to C=O stretching vibration at 1713 cm<sup>-1</sup> confirming the formation of GO NSs, as indicated in the XRD analysis. Fig. 3 shows that the C=O peak grew as the GO NSs weight percent ratio rose, reaching its highest intensity for SG3 (GO NSs = 0.01 wt%) and resulting in a more hydrophilic membrane surface.<sup>71</sup> Then the intensities of the peaks decrease with any further addition of GO NSs. The presence of boarding peaks confirmed the successful incorporation of GO NSs in the polymer matrix. There are other many peaks observed in the IR spectrum related to PES. The peak around 1295 cm<sup>-1</sup> is arising due to O=S=O asymmetric stretching, whereas the symmetric stretching of O-S-O gives a band at around 1150 cm<sup>-1</sup>. The bands at around 1240 cm<sup>-1</sup> and 1040 cm<sup>-1</sup> are characteristic peaks corresponding to asymmetric and symmetric stretching vibrations of the C-O-C group, respectively. Also, peaks between 2900 cm<sup>-1</sup> and 3100 cm<sup>-1</sup> correspond to aromatic and aliphatic C-H stretching vibrations.<sup>72</sup>

#### 3.2.2. Surface morphology

##### 3.2.2.1 SEM analysis of PES/GO MMW FO membranes.

Fig. 4 shows FE-SEM images of top, bottom, and cross-section



surfaces of PES/GO MMW membranes with different wt% ratios of GO NSs. Fig. 4(A–E) shows significant differences between the surface images of the bare PES and blended PES/GO MMW membranes. The FE-SEM images clearly showed that GO NSs immigrate to the top and bottom surfaces of the membranes. A possible explanation for this can be given based on the hydrophilic nature of GO NSs. The hydrophilic nature of GO NSs is responsible for the fast exchange of solvent and non-solvent during the phase inversion process which leads to extended porosity as well as changes in the macro-void structure.<sup>73,74</sup> In addition, as seen from the FE-SEM image, GO NSs with weight

ratios ranging from zero to 0.1 wt% were well dispersed in the polymer matrix. Also, at a higher GO NSs wt% ratio, we noticed the presence of GO NSs agglomeration at the membrane surface which is attributed to the carbon-based structure of GO NSs as shown in Fig. 4(D and E).

The cross-section images of the prepared nanocomposite membranes indicated that the structural morphology was greatly affected by the addition of GO NSs (Fig. 4). The cross-section of bare PES, Fig. 4(A) is an individual micro void structure, which is drastically altered by the addition of GO NSs to the polymer matrix during the phase separation process, Fig. 4(B). These macro-voids extended from the top surface to the bottom with increasing GO NSs wt% ratio till SG3 (0.01 wt%) in Fig. 4(C). By adding GO NSs with a weight ratio larger than 0.01 wt%, the GO NSs are aggregated, and macro-voids are converted to layer structure (SG6 with 0.1 wt%) as shown in Fig. 4(E). Double skin-layer structures were developed after loading GO NSs higher than 0.01 wt% ratio as shown in Fig. 4(E), which in turn, enhances the water permeability.<sup>75</sup> These results completely agreed with AFM measurements as illustrated in Fig. 5 and listed in Table 2.

In general, all PES membranes with or without GO NSs displayed asymmetric porous sub-layer structure with a dense top-layer and porous layer at the middle and bottom structure. Also

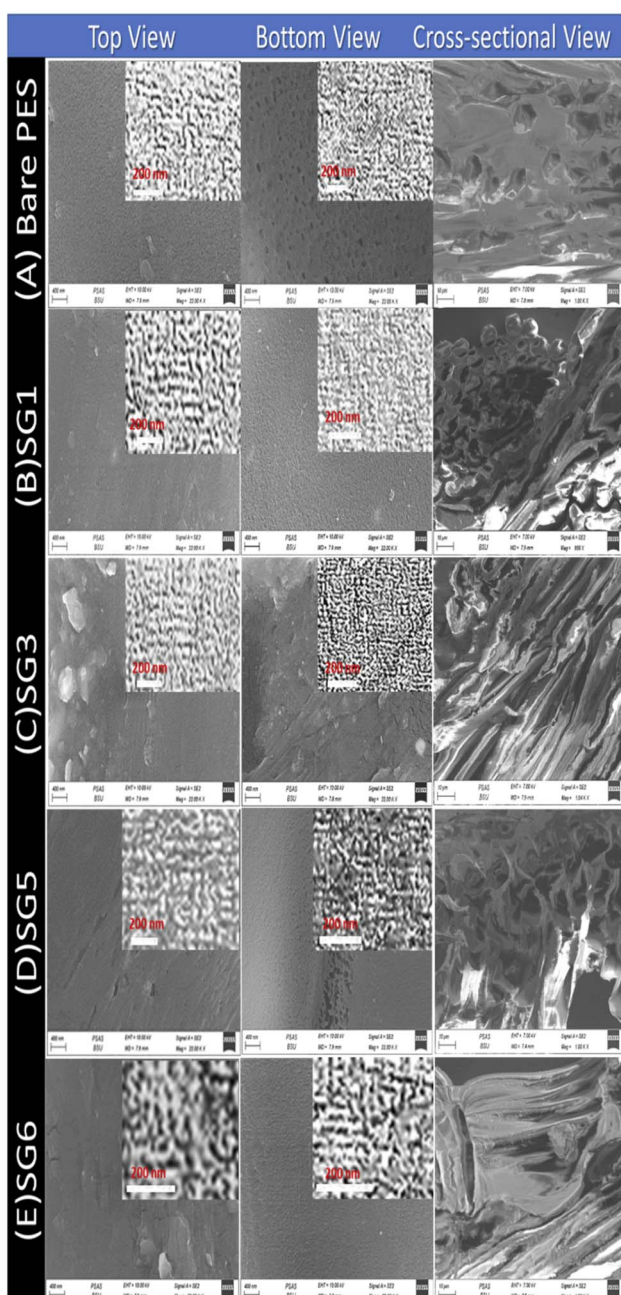


Fig. 4 Top, bottom, and cross-sectional SEM images of PES/GO MMW FO membranes with different GO NSs wt% ratios.

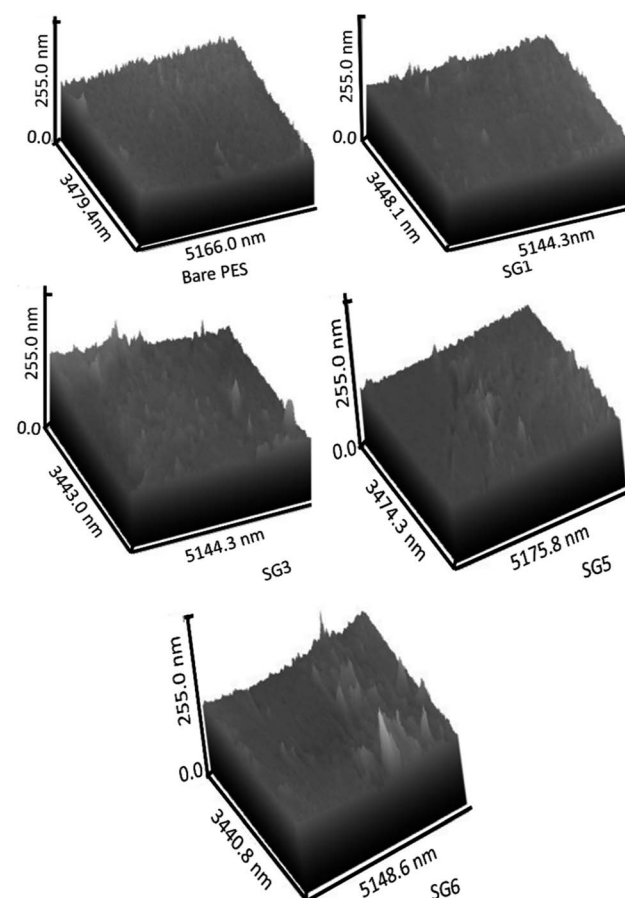


Fig. 5 3D AFM images of the prepared PES/GO MMW FO membranes with different GO NSs wt%.



**Table 2** Surface roughness parameters of the prepared PES/GO MMW FO membranes prepared with different GO NSs wt%

Sample	$R_a$ (nm)		$R_q$ (nm)	
	Top	Bottom	Top	Bottom
Bare PES	23.38	23.66	24.37	24.52
SG1	23.55	24.11	24.46	24.77
SG3	24.25	24.72	24.83	25.08
SG5	24.29	24.75	24.86	25.1
SG6	24.46	24.46	24.92	24.92

as shown in the insets of Fig. 4(A–C), the pore size decreases from virgin PES membrane to SG3 membrane. After that, the pore size increases with increasing GO NSs wt% at SG5 and SG6 membranes, insets of Fig. 4(D and E). This finding implies that when the weight% ratio of GO NSs increases, the hydrophilic character of GO NSs improves. It also refers to the coagulation step's enhancement of the mass exchange rate between solvent and non-solvent, allowing for the creation of wider pore channels. This is consistent with IR studies, which showed a broad characteristic stretching band of the hydroxyl group between 3100 and 3600  $\text{cm}^{-1}$ .

**3.2.2.2. AFM analysis and roughness parameters.** The three-dimensional AFM image of the nanocomposite membranes surface is shown in Fig. 5. Concerning surface roughness, as shown in AFM images of Fig. 5, the surface roughness of PES/GO MMW membranes was increased from 23.38 to 24.46 nm and bottom roughness was increased from 23.66 to 24.75 by an increase in GO NSs loading from zero to 0.1 wt%. The creation of a double-skinned layer PES/GO MMW FO membrane is shown by the sample SG6 roughness of the top and bottom being equal. This result is most likely due to the hydrophilic character of GO NSs, which accelerated phase exchange during the phase inversion process, allowing these nanoparticles to migrate to the membrane surface and bottom. According to AFM results, it could be concluded that GO NSs were significantly incorporated on the membrane surface. The surface

roughness parameters of the prepared membrane are presented in Table 2. The  $R_a$  parameter represents the mean roughness of the scanning surface, and  $R_q$  is the mean square root roughness. From Table 2, the addition of GO NSs changes the roughness of the PES membrane.  $R_a$  value increases may lead to flux augmentation, which is followed by an increase in the area accessible for water transport, surface pore diameter, mechanical strength, and thermal stability. Also, the surface roughness of the membrane is a very effective parameter in its antifouling features. An essential feature of nanofiller addition in polymeric solution is that it increases the viscosity of the solution as the nanoparticle loading increases. Although the viscosity of polymeric solutions was not tested experimentally, the addition of GO NSs changed the viscosity of polymeric casting solution. Many publications on this phenomenon claim that increased viscosity causes lateral holes to form, similar to the pores seen in this study.<sup>76,77</sup>

**3.2.3. Membrane physical properties.** Table 3 shows the influence of GO NSs wt% on membrane physical parameters such as water uptake%, porosity, contact angle, thickness, and tortuosity of PES/GO MMW FO membranes manufactured with total casting thickness of 215  $\mu\text{m}$  and 265  $\mu\text{m}$ .

**3.2.3.1. Water contact angles.** The contact angle parameter is used to study the wettability (hydrophilicity) of the membrane surface. Contact angles are evaluated and documented in Table 3 to investigate the influence of GO NSs loading on the hydrophilicity of PES/GO MMW FO membranes. The contact angle of the bare PES membrane was 76°, and the contact angle dropped to roughly 55° when the wt% ratio of loading GO NSs was increased from 0 to 0.1 wt% at a total casting thickness of 215  $\mu\text{m}$ . Due to the hydrophilic characteristic of GO, the PES/GO MMW membranes exhibit a significant increase in membrane surface hydrophilicity when compared to pristine PES membranes.<sup>78,79</sup> Also, as noted in SEM images and reported in prior literature, this enhancement in hydrophilicity might be attributable to the migration of loaded GO to the membrane surfaces during phase inversion processes.<sup>59,80</sup>

**Table 3** Effect of GO NSs wt% on the water uptake%, porosity%, contact angle, thickness, and tortuosity of PES/GO MMW FO membranes prepared using total casting thickness of (A) 215  $\mu\text{m}$  and (B) 265  $\mu\text{m}$ 

Samples	GO NSs wt% ratio	Water uptake (%)	Porosity (%)	Contact angle (degree)	Thickness ( $\mu\text{m}$ )	Tortuosity ( $\tau$ )
<b>Total casting thickness = 215 <math>\mu\text{m}</math></b>						
Bare PES	0	35	40	76	$149 \pm 4.4$	6.4
SG1	0.004	47	56	74	$151 \pm 4.5$	3.7
SG2	0.008	48	59	69	$155 \pm 4.6$	3.3
SG3	0.01	49	62	65	$159 \pm 4.7$	3
SG4	0.04	51	60	60	$160 \pm 4.8$	3.2
SG5	0.08	53	59	58	$162 \pm 4.8$	3.3
SG6	0.1	55	54	55	$167 \pm 5.0$	3.9
<b>Total casting thickness = 265 <math>\mu\text{m}</math></b>						
Bare PES	0	34	32	72	$163 \pm 4.8$	8.82
SG1	0.004	35	39	70	$156 \pm 4.6$	6.6
SG2	0.008	36	41	65	$158 \pm 4.7$	6.1
SG3	0.01	42	47	58	$162 \pm 4.8$	4.9
SG4	0.04	44.5	43	57	$177 \pm 5.3$	5.7



**3.2.3.2 Membrane water uptake and porosity.** Water uptake and porosity of constructed PES/GO MMW membranes are primarily determined by two factors: (1) the number of hydrophilic sites in the membrane matrix, and (2) the membrane surface shape, particularly the existence of macro voids in the polymeric sub-layer. According to Table 3, increasing hydrophilicity (*i.e.*, lowering the contact angle) improves water uptake. With increasing the wt% ratio of loaded GO NSs from zero to 0.1%, the contact angle decreased from 76° to 55°, and the water uptake increased from 35% to 55%. This increase in water uptake may be explained by the fact that the PES MMW membrane's affinity for water rises when the GO NSs include more hydrophilic sites, allowing for easier water uptake into the membrane matrix.<sup>72</sup> In addition, because GO NSs create holes and macro voids in sub-layers of the polymer matrix, allowing more water to be absorbed, the PES/GO membrane may take more water molecules and therefore increase the water uptake capacity.<sup>81,82</sup>

For the porosity of PES/GO MMW membranes, as the GO NSs wt% ratio increased from zero to 0.01% (SG3), the porosity increased from 40% to 62% and then decreased to 54% for 0.1 GO wt% (SG6). This suggests that SG3 (0.01 GO NSs wt%) has the largest porosity, which enhances the internal structure of the membrane, increasing its properties and perhaps leading to increased directional flow rates across the SG3 membrane.<sup>83,84</sup> When loaded GO NSs more than 0.01 wt percent, the agglomerated internal structures that extended from the top surface to the bottom surface of the membrane to generate layer structure (Fig. 4) are responsible for the decrease in porosity.

**3.2.3.3 Membrane thickness, tortuosity, and *S* value.** As the wt% ratio of GO NSs was raised from 0 to 0.1% for 215 µm total casting thickness, the thickness of manufactured PES/GO MMW FO membranes was increased from 149 to 167 µm. The rise in membrane thickness is linked to the increase in the viscosity of the GO-doped casting solution. An essential feature of nanofiller addition in polymeric solution is raising the viscosity of the solution owing to the increase of the GO NSs wt% loading.<sup>58,85</sup> Based on the characteristics of fabricated membranes in Table 3, the tortuosity ( $\tau$ ) of the membrane substrate was estimated. The tortuosity values of bare PES, PES/0.01%GO MMW, and HTI CTA membrane were 6.4, 3.0, and 4.75, respectively. The low tortuosity value of PES/0.01% GO MMW membrane is attributed to the larger open area of mesh woven fabric, which allows the polymer to permeate the substrate's bottom layer and form open pores, as seen in SEM images (Fig. 4).<sup>75</sup>

Table 4 compares our optimized membrane to three cellulosic commercials woven FO membranes in terms of *S* value and

tortuosity.<sup>75,85,86</sup> In FO studies, the *S* value has been widely used to express the degree of ICP effects of the substrate.<sup>75</sup> Eqn (4) clarifies the relationship between the structural parameter, porosity, and tortuosity. The SG3 MMW FO membrane has low tortuosity and high porosity due to its sponge-like structure, resulting in a small *S* value of 149 µm when compared to the commercial membranes. The smallest *S* value for SG3 resulted in the ICP impact being minimized and FO performance being improved. Because of the use of a woven mesh with a wide-open area, water flow is facilitated, as seen by the membrane substrates' decreased tortuosity ( $\tau = 3$ ), increased porosity, and wettability.<sup>87,88</sup> As a result, the SG3 membrane is projected to outperform several commercial membranes in FO applications, including the CTA membrane, as demonstrated in Table 4.

### 3.3. Membrane performance

**3.3.1. Effect of total casting height on PES/GO MMWFO membrane performance.** The casting height has a significant impact on the performance of the PES/GO MMW FO membrane. As a result, it's critical to investigate the impact of total casting height on the performance of the FO membrane. The performance of the constructed PES/GO MMW FO membranes was investigated at two common total casting heights (215 and 265 µm), as shown in Fig. 6(A) and the data reported in Table 5. The highest water flux of the membrane prepared at the optimum conditions (SG3, GO 0.01 wt%) was 114.7 LMH and 65 LMH at total casting heights of 215 and 265 µm, respectively, Fig. 6(A). At the same time, it was found that there is a slight increase in reverse salt flux (RSF) from 0.025 to 0.030 GMH decreasing the total casting thickness from 265 to 215 µm for the optimal membrane, as recorded in Table 5. This might be explained by the fact that the overall casting thickness of the membrane is lower, and the membrane permeability is higher (higher porosity).<sup>89</sup> Hence, the SG3 with the smallest thickness produces the highest membrane permeability and selectivity as indicated by the lowest specific reverse salt flux ( $J_s/J_w = 0.00026 \text{ g L}^{-1}$ ).

**3.3.2. Effect of different GO NSs wt% ratio on PES/GO MMWFO membrane performance.** The effect of GO NSs wt% ratio on PES/GO MMW FO membrane performance is shown in Fig. 6(A). The FO water and salt fluxes are estimated in FO mode using NaCl (1 M) as a draw solution and distilled water as a feed solution in FO mode.

From Fig. 6(A), for 215 µm total casting height, the water flux increased from 60 LMH to 114.7 LMH by increasing GO NSs wt% ratio from zero to 0.01 wt%. After that, the water flux decreases to 70 LMH and 41.8 LMH at 0.04 and 0.1 GO NSs wt%

Table 4 Structural parameters and tortuosity of different membranes

Membrane	<i>S</i> (µm)	$\tau$	Ref.
PES/GO MMWFO (0.01 wt% GO NSs)	149	3	This work
HTI-CTA	811	4.75	75
CTA-HW (cellulose triacetate with polyester highly woven fabric)	720	—	85
TFCGO (0.0175)	274	—	86



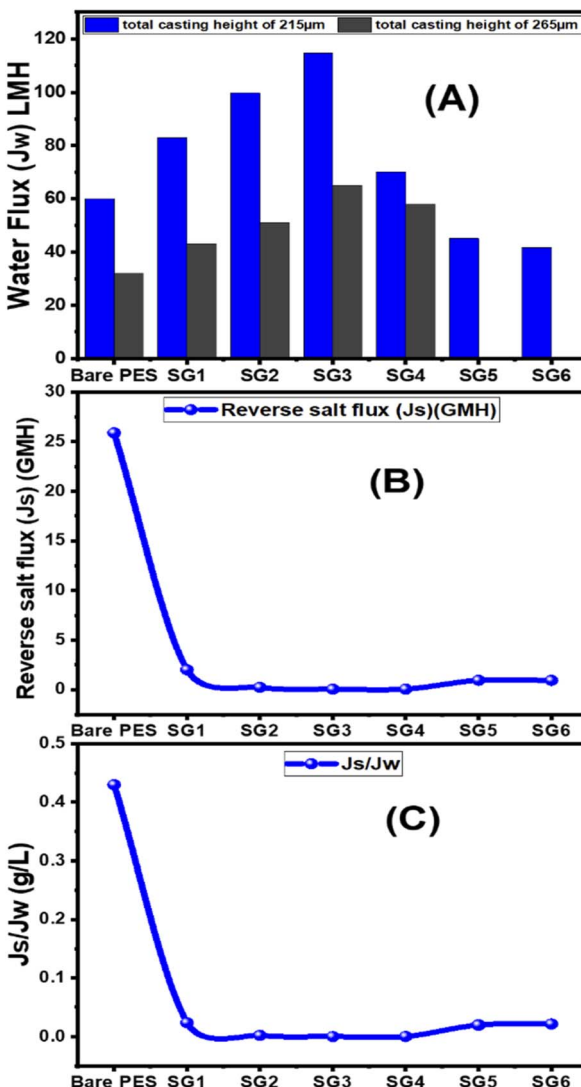


Fig. 6 PES/GO MMW FO membranes performance indicators; variation of (A) the water flux ( $J_w$ ) for the prepared membranes using 215  $\mu\text{m}$  and 265  $\mu\text{m}$  total casting thicknesses; (B) the minimum reverse salt flux ( $J_s$ ) and (C)  $J_s/J_w$  for the prepared membranes using 215  $\mu\text{m}$  total casting thickness versus the GO NSs wt%.

ratio, respectively. At 265  $\mu\text{m}$  total casting thickness, the water flux increased from 32 LMH to 65 LMH by increasing the wt% ratio of GO NSs from zero to 0.01 wt% then water flux decreased to 58 LMH at 0.04 GO NSs wt% ratio. Many factors contributed to the increase in water flow when the GO NSs wt percent ratio was increased: incorporation of GO NSs layers distributed the polymer backbone chain, and the presence of OH groups increased the hydrophilicity of the PES/GO MMW surface. The overall porosity and water flow increase as the loaded GO NSs reach 0.01 wt percent ratio (SG3), owing to a decrease in the  $S$  value, which minimizes the internal concentration polarization ICP.<sup>81,82,89,90</sup> But, for loading GO NSs higher than 0.01 wt% ratio, the water flux decreased. This may be attributed to the agglomeration of GO NSs on the surface of the PES membrane.<sup>25,91,92</sup> According to these results, the optimum total casting height has been chosen to be 215  $\mu\text{m}$  for further FO performance study.

The effect of GO NSs wt% ratio on the reverse salt flux ( $J_s$ ) and  $J_s/J_w$  for the prepared membranes using 215  $\mu\text{m}$  total casting thickness are estimated and plotted in Fig. 6(B and C). The minimum reverse salt flux ( $J_s$ ) of 0.03 GMH was obtained at a 0.01 wt% ratio GO NSs as compared with pristine PES membrane 25.9 GMH. Then, any further increase in GO NSs wt% ratio is accompanied by increasing in  $J_s$  to reach a maximum of 0.9 GMH at a higher GO NSs of 0.08 and 0.1 wt% ratio due to the increase in pore size as shown from SEM analysis. The SRSF ( $J_s/J_w$ ) is often used as a more reliable parameter for evaluating the properties of the FO membranes to reverse the diffusion of draw solutes. This ratio is applied to measure the volume of draw solute loss per unit of water passed through the membrane. Lower  $J_s/J_w$  is desirable to prevent the loss of draw solutes in FO and help to minimize ICP.<sup>93</sup>  $J_s/J_w$  of PES/GO WMM FO membranes prepared are decreased with increasing GO NSs from 0.004 to 0.01 wt% ratio, then there are slightly increase of ( $J_s/J_w$ ) with increasing GO NSs from 0.08 to 0.1 wt% ratio. The lower SRSF values are essential for the FO membranes as this means a reduction in the loss of draw solutes from the process which has both economic and environmental implications. The lower SRSF data shows that GO NSs incorporation within the substrate could significantly enhance the water flux and ion selectivity (higher water flux and

Table 5 FO membrane performance indicators for PES/GO MMW membranes of total casting thicknesses 215 and 265  $\mu\text{m}$

Membrane ID	Membrane total casting thickness							
	215 $\mu\text{m}$		265 $\mu\text{m}$		Flux ( $J_w$ ) LMH	Reverse ( $J_s$ ) GMH	$J_s/J_w$ ( $\text{g L}^{-1}$ )	Salt rejection%
	Flux ( $J_w$ ) LMH	Reverse ( $J_s$ ) GMH	$J_s/J_w$ ( $\text{g L}^{-1}$ )	Salt rejection%				
Bare PES	60.0	25.9	0.43	$53 \pm 1.5$	32	7.5	0.23	$85 \pm 2.5$
SG1	83.0	2.0	0.024	$94 \pm 2.8$	43	0.21	0.0048	$98.5 \pm 2.9$
SG2	99.7	0.22	0.0022	$98 \pm 2.4$	51	0.18	0.0035	$98.7 \pm 2.9$
SG3	114.7	0.03	0.00026	$99 \pm 2.9$	65	0.025	0.00038	$99.5 \pm 3$
SG4	70.0	0.04	0.00057	$98.8 \pm 2.9$	58	0.05	0.00086	$98.8 \pm 2.9$
SG5	45.0	0.93	0.02	$96.2 \pm 2.8$	—	—	—	—
SG6	41.8	0.92	0.022	$95.7 \pm 2.9$	—	—	—	—



lower RSF) thereby lowering the SRSF PES/GO MMW of the membranes.<sup>22</sup>

**3.3.3 Effect of time on SG3 PES/GO MMW FO membrane performance.** The impacts of run time on FO membrane performance indicators, water flow ( $J_w$ ) and reverse salt flux ( $J_s$ ), were explored for the optimum membrane SG3 PES/GO MMW, as illustrated in Fig. 7. After 0.166 h, the highest water flux value (161 LMH) was reached, followed by a fast fall to 56 LMH at 0.33 h, and finally, as shown in Fig. 7(A), the water flux consents up to 35 LMH with any additional increase in time. Water flux was initially maximum due to enhanced osmotic pressure, however, this dropped over time due to permeate flow dilution of the draw solution, resulting in flux reductions. Fig. 7(B) also shows that the reverse salt flux follows the same temporal behavior as the water flux. The higher flux may be attributed that the formation of a double-skinned layer FO membrane. The rapid decrease noted in Fig. 7 was attributed to the occurrence of external concentration polarization (ECP) on the feed side and internal concentration polarization on the draw side.<sup>53</sup>

**3.3.4. Effects of varying NaCl concentrations on the performance of the SG3 PES/GO MMW FO membrane.** Using the FO system with various draw NaCl solutions of concentrations ranging from 0.6 to 2 M and distilled water as feed solution, the performance of the PES/GO MMWFO (SG3) membrane manufactured at the optimal condition (0.01% GO NSs wt%, total casting thickness of 215  $\mu$ m) was investigated. Fig. 8(A) demonstrated that the water flux increases gradually and the water flux of the prepared PES/GO MMWFO membrane is much higher than that of the woven commercial cellulose triacetate (CTA) membrane. For comparison, as the NaCl concentration changed from 0.6 to 2 M, the water flux of the prepared membrane ranged between 105 to 127 LMH, while the commercial membrane water flux ranged from 7.2 LMH to 15 LMH. The increase in water flux can be attributed to the fact that osmotic pressure rises as salt concentration rises.<sup>94</sup> Many researchers have discovered that when water passes through the asymmetric FO membrane from the feed solution to the draw solution, it dilutes salts inside the porous support layer, resulting in a gradual increase in water flow.<sup>95,96</sup> Under the optimal FO conditions, the enhanced membrane performs significantly better than the commercial cellulose triacetate (CTA) woven control membrane. This is ascribed to a number of

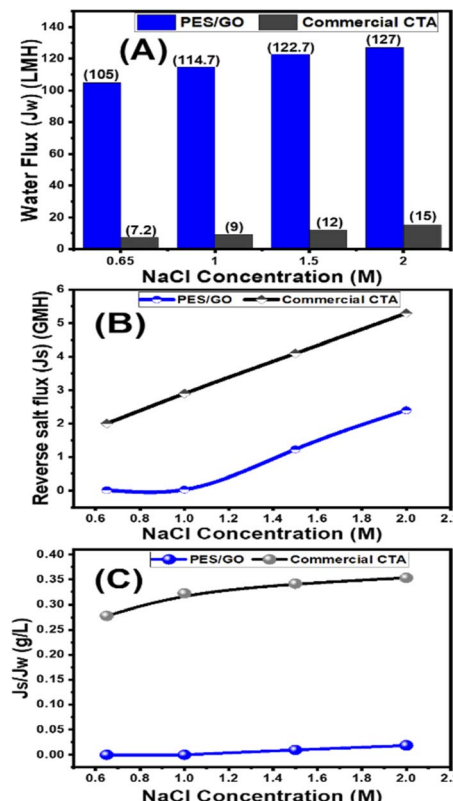


Fig. 8 Comparison of the (A) water flux ( $J_w$ ), (B) reverse salt flux ( $J_s$ ), and (C)  $J_s/J_w$  of the prepared PES/GO MMW FO membrane (SG3) with the woven commercial cellulose triacetate (CTA) membrane as a function of the NaCl concentration. Measurements were carried out at the same conditions.

variables, many of which depend on the presence of GO ultra-thin NSs multilayers that disperse and disseminate throughout the polymer backbone chain during preparation and cast on an open area woven fabric. The presence of functional groups including OH, COOH, and carbonyl groups enhanced the hydrophilicity (reduction in WCA) of the PES/GO MMW surfaces and the interfacial interactions between them. The overall membrane porosity and wetness increase, and water flow rise as the loaded GO NSs expand. Additionally, the MMM WFO membrane created under optimum conditions has a lower *S* structure value (149  $\mu$ m) than CTA; this decrease in *S* structure reduces the internal concentration polarization, or ICP, to a minimum. All of these characteristics result in improved membrane performance. Increasing the NaCl concentration from 0.6 to 2 M also resulted in a modest increase in reverse salt flux for the SG3 membrane, from 0.017 to 2.4 GMH, as shown in Fig. 8(B). The SRSF ( $J_s/J_w$ ) is one of the important FO performance parameters, so this parameter is calculated for fabricated and commercial membranes and plotted in Fig. 8(C). A low  $J_s/J_w$  value is desirable for minimizing reverse salt diffusion, avoiding excessive membrane fouling, and reducing draw solute replenishment costs. The lower SRSF of the PES/GO MMW membrane compared to the woven CTA membrane is most likely due to the integration of GO in the membrane

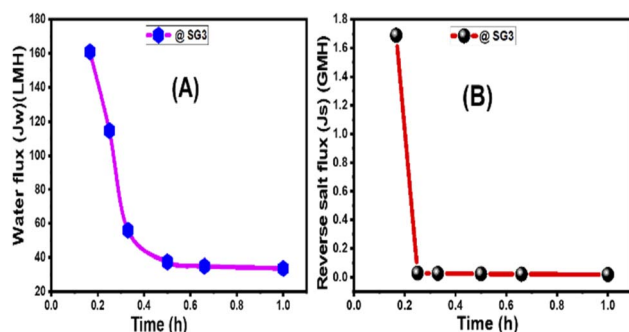


Fig. 7 Effect of run time on PES/GO MMW FO membrane (SG3) performance; (A) water flux ( $J_w$ ) and (B) reverse salt flux ( $J_s$ ).



substrates, which improves water permeability by increasing porosity and wettability.

The mechanical properties of the membranes were also strengthened by the incorporation of GO nanosheets. The mechanical properties measurements show that PES/GO MMWFO membrane has a tensile strength of 45 MPa, which is higher than the strength of the commercial CTA woven FO membrane, which is 35.8 MPa. The elongation% was 19% and 37.8% for PES/GO MMW and the commercial CTA woven FO membranes, respectively. The tensile strength increases once the GO nanosheets are applied, going from 12 MPa for PES to about 45 MPa for the PES/GO MMW membrane. The incorporation of hydrophilic inorganic nano-sheets, like GO, can improve the surface hydrophilicity, thermal and mechanical stability, and anti-fouling property of hybrid membranes, according to research by Zhu *et al.*<sup>97</sup> This is because GO has an exceptional ability to combine the processability of the polymer with the superior properties of the 2D materials. The antifouling and subsequent permeation capabilities of PES are improved by GO nano-sheet blending at 0.01 percent (as demonstrated by hydrophilicity, water uptake rate, contact angle, reduced *S* structure, and lower ICP), which extends the membrane's lifespan and lowers its operational costs.<sup>98–100</sup> Incorporation of GO for membrane preparation could be therefore a promising alternative for improving substrate properties of the PES/GO MMW membranes due to the formation of double skin layer membrane.

**3.3.5 Salt rejection.** Fig. 9 shows the salt rejection efficiency of both the woven CTA membrane and our optimized membrane (SG3, 215  $\mu$ m). From Fig. 9, it was observed that the salt rejection of our prepared membrane decreased from 99.2% @0.65 M to 98%@2 M, whereas the salt rejection of the commercial membrane changed from 97% to 90% at the same range of NaCl concentration. This means that the salt rejection of our membrane is higher than the salt rejection of the woven CTA membrane. The lowered *S* parameter, tortuosity, and  $J_s/J_w$  of our PES/GO MMW may explain its superior salt rejection. For

adsorption and separation, also, the inclusion of GO enhances membrane porosity and active sites. As shown in Table 5, the salt rejection increases from 53% to 99% and from 85 to 99.5% for the total casting height of 215 and 265  $\mu$ m, respectively. These results show that SG3 with the highest total casting membrane thickness (265  $\mu$ m) reduced water transportation rate (flux 65 LMH) due to the increase in *S*-structure which leads to ICP. These results agree with the literature.<sup>37,101</sup>

## 4. Conclusion

Graphene oxide nanosheets (GO NSs) produced utilizing a modified Hummer's technique were characterized using SEM, TEM, EDX, XRD, and Raman. By introducing different wt% ratios of GO NSs (zero to 0.1 wt%) into the polyethersulfone (PES)/matrix, mixed matrix woven forward osmosis (MMWFO) membranes were produced using the phase inversion method. Water contact angle, hydrophilicity, porosity, tortuosity, function groups, chemical and crystallographic structures, nano-morphologies, and surface roughness of the produced PES/GO MMWFO membranes have been investigated. The produced PES/GO FO membranes were assessed in terms of pure water flux ( $J_w$ ), reverse salt flux ( $J_s$ ), and salt rejection for water desalination. With the addition of GO NSs, the hydrophilicity and porosity of the FO membrane improved, as did water permeability due to the creation of numerous skin-layer structures with increased GO NSs loading. The water contact angle is decreased to 55° by increasing the GO NSs wt% to 0.1%, whereas the highest porosity reached 62% at 0.01%. These GO NSs create shortcut paths for water molecules to travel through, reducing support layer tortuosity by three times, lowering structural characteristics of the support layer, and diminishing internal concentration polarization (ICP). For bare PES, the values of  $J_w$ ,  $J_s$ , and RS were 60 LMH, 25.9 GMH, and 53%, respectively. With the highest  $J_w$  (114.7 LMH), lowest  $J_s$  (0.03 GMH), and lowest specific reverse solute flux ( $J_s/J_w = 0.00026$  g L<sup>-1</sup>), as well as a more favorable structural parameter ( $S = 148$  m), the PES/0.01 wt% GO MMWFO membrane with a total casting thickness of 215  $\mu$ m and 1 M NaCl concentration had the best performance. Under ideal FO circumstances, the performance of our improved membrane outperforms that of the control woven commercial cellulose triacetate (CTA) FO membrane.  $J_w$  grew from 105 to 127 LMH as the NaCl concentration increased from 0.6 to 2 M, which is substantially greater than the commercial  $J_w$  (7.2 to 15 LMH). The SR of our FO membranes is 99.2%@0.65 M NaCl, which is much higher than that of the CTA membrane.

## Author contributions

Conceptualization, M. N., N. A., S. S. A., H. M. A. and M. S.; methodology, M. N., N. A., S. S. A. and M. S.; validation, M. N., S. S. A., H. M. A., and M. S.; formal analysis, M. N., N. A., S. S. A., and M. S.; investigation, M. N., S. S. A., and M. S.; resources, M. N., N. A., S. S. A., and M. S.; data curation, M. N., H. M. A. and M. S.; writing—original draft preparation, M. N., S. S. A., and M. S.; writing—review and editing, M. N., N. A., S. S. A., and M. S.

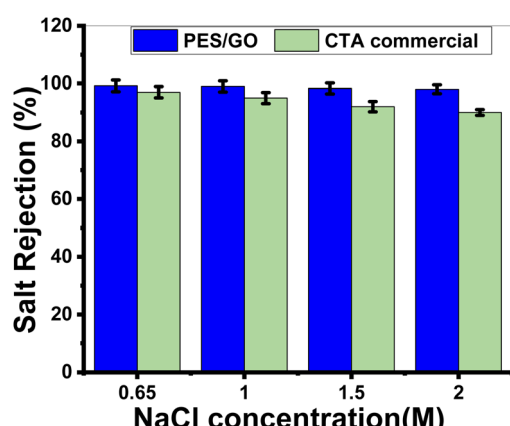


Fig. 9 Salt rejection efficiency of the fabricated SG3 FO membrane and the commercial cellulose triacetate (CTA) membrane. The error bars are provided based on triplicate measurements. Measurements were carried out at the same conditions.



A., and M. S.; visualization, M. N., N. A., S. S. A., H. M. A., and M. S.; project administration, N. A. M. N. and M. S.; funding acquisition, M. N., N. A., and M. S. All authors have read and agreed to the published version of the manuscript.

## Conflicts of interest

The authors declare no conflict of interest.

## Acknowledgements

Princess Nourah bint Abdulrahman University Researchers Supporting Project number (PNURSP2022R291), Princess Nourah bint Abdulrahman University, Riyadh, Saudi Arabia. Additionally, this research received external funding from the Egyptian Academy of Scientific Research and Technology, which partially supported this work (ASRT/SNG/W/2018-10). The authors express their gratitude to Princess Nourah bint Abdulrahman University Researchers Supporting Project number (PNURSP2022R291), Princess Nourah bint Abdulrahman University, Riyadh, Saudi Arabia. Additionally, the authors gratefully acknowledge the financial support from the Egyptian Academy of Scientific research and Technology, which partially supported this work (ASRT/SNG/W/2018-10).

## Notes and references

- 1 M. Shaban, A. M. Ashraf, H. AbdAllah and H. M. Abd El-Salam, *Desalination*, 2018, **444**, 129–141.
- 2 A. Krell and H. Ma, *J. Am. Ceram. Soc.*, 2003, **86**, 241–246.
- 3 M. R. Bilad, E. Guillen-Burrieza, M. O. Mavukkandy, F. A. Al Marzooqi and H. A. Arafat, *Desalination*, 2015, **376**, 62–72.
- 4 K. Y. Wang, T. Matsuura, T. S. Chung and W. F. Guo, *J. Membr. Sci.*, 2004, **240**, 67–79.
- 5 U. K. Garg, M. P. Kaur, D. Sud and V. K. Garg, *Desalination*, 2009, **249**, 475–479.
- 6 M. Pinelo, G. Jonsson and A. S. Meyer, *Sep. Purif. Technol.*, 2009, **70**, 1–11.
- 7 M. G. Khedr, *Desalination*, 2003, **153**, 295–304.
- 8 S. Yang, Q. Zou, T. Wang and L. Zhang, *J. Membr. Sci.*, 2019, **569**, 48–59.
- 9 R. Mahendran, R. Malaisamy and D. R. Mohan, *Polym. Adv. Technol.*, 2004, **15**, 149–157.
- 10 M. S. Shalaby, H. Abdallah, A. Cenian, G. Sołowski, M. Sawczak, A. M. Shaban and R. Ramadan, *Sep. Purif. Technol.*, 2020, **247**, 116994.
- 11 M. Shaban, H. AbdAllah, L. Said, H. S. Hamdy and A. Abdel Khalek, *Chem. Eng. Res. Des.*, 2015, **95**, 307–316.
- 12 F. Valentini, A. Calcaterra, V. Ruggiero, D. Giacobbe and M. Botta, *JSM Nanotechnol. Nanomed.*, 2018, **6**, 1060.
- 13 Q. Saren, C. Q. Qiu and C. Y. Tang, *Environ. Sci. Technol.*, 2011, **45**, 5201–5208.
- 14 W. L. Ang, A. Wahab Mohammad, D. Johnson and N. Hilal, *J. Water Proc. Eng.*, 2019, **31**, 100886.
- 15 K. Lutchmiah, L. Lauber, K. Roest, D. J. H. Harmsen, J. W. Post, L. C. Rietveld, J. B. van Lier and E. R. Cornelissen, *J. Membr. Sci.*, 2014, **460**, 82–90.
- 16 A. J. Ansari, F. I. Hai, W. Guo, H. H. Ngo, W. E. Price and L. D. Nghiem, *Bioresour. Technol.*, 2015, **191**, 30–36.
- 17 A. Altaee and A. Sharif, *Desalination*, 2015, **356**, 31–46.
- 18 A. Achilli, T. Y. Cath and A. E. Childress, *J. Membr. Sci.*, 2009, **343**, 42–52.
- 19 X. Li, S. Chou, R. Wang, L. Shi, W. Fang, G. Chaitra, C. Y. Tang, J. Torres, X. Hu and A. G. Fane, *J. Membr. Sci.*, 2015, **494**, 68–77.
- 20 E. M. Garcia-Castello and J. R. McCutcheon, *J. Membr. Sci.*, 2011, **372**, 97–101.
- 21 D. L. Shaffer, J. R. Werber, H. Jaramillo, S. Lin and M. Elimelech, *Desalination*, 2015, **356**, 271–284.
- 22 M. J. Park, S. Phuntsho, T. He, G. M. Nisola, L. D. Tijing, X. M. Li, G. Chen, W. J. Chung and H. K. Shon, *J. Membr. Sci.*, 2015, **493**, 496–507.
- 23 M. Shatat and S. B. Riffat, *Int. J. Low-Carbon Technol.*, 2014, **9**, 1–19.
- 24 E. Ali, J. Orfi, A. Najib and J. Saleh, *PLoS One*, 2018, **13**(10), e0205012.
- 25 T. Sirinupong, W. Youravong, D. Tirawat, W. J. Lau, G. S. Lai and A. F. Ismail, *Arabian J. Chem.*, 2018, **11**, 1144–1153.
- 26 B. Kim, G. Gwak and S. Hong, *Desalination*, 2017, **422**, 5–16.
- 27 R. K. McGovern and J. H. Lienhard V, *J. Membr. Sci.*, 2014, **469**, 245–250.
- 28 W. A. Suwaileh, D. J. Johnson, S. Sarp and N. Hilal, *Desalination*, 2018, **436**, 176–201.
- 29 S. Phuntsho, H. K. Shon, T. Majeed, I. El Saliby, S. Vigneswaran, J. Kandasamy, S. Hong and S. Lee, *Environ. Sci. Technol.*, 2012, **46**, 4567–4575.
- 30 P. Xiao, L. D. Nghiem, Y. Yin, X. M. Li, M. Zhang, G. Chen, J. Song and T. He, *J. Membr. Sci.*, 2015, **481**, 106–114.
- 31 M. J. Park, S. Phuntsho, T. He, G. M. Nisola, L. D. Tijing, X. M. Li, G. Chen, W. J. Chung and H. K. Shon, *J. Membr. Sci.*, 2015, **493**, 496–507.
- 32 G. Chen, Z. Wang, L. D. Nghiem, X. M. Li, M. Xie, B. Zhao, M. Zhang, J. Song and T. He, *Desalination*, 2015, **366**, 113–120.
- 33 H. Li, Y. Gao, Y. Shao, Y. Su and X. Wang, *Nano Lett.*, 2015, **15**, 6689–6695.
- 34 J. Deng, X. Liu, L. Ma, C. Cheng, W. Shi, C. Nie and C. Zhao, *ACS Appl. Mater. Interfaces*, 2014, **6**, 21603–21614.
- 35 W. Suwaileh, N. Pathak, H. Shon and N. Hilal, *Desalination*, 2020, **485**, 114455.
- 36 S. Zhao, Z. Wang, J. Wang, S. Yang and S. Wang, *J. Membr. Sci.*, 2011, **376**, 83–95.
- 37 J. Su and T. S. Chung, *J. Membr. Sci.*, 2011, **376**, 214–224.
- 38 C. Klaysom, T. Y. Cath, T. Depuydt and I. F. J. Vankelecom, *Chem. Soc. Rev.*, 2013, **42**, 6959–6989.
- 39 A. Tiraferri, N. Y. Yip, W. A. Phillip, J. D. Schiffman and M. Elimelech, *J. Membr. Sci.*, 2011, **367**, 340–352.
- 40 M. Shaban, A. M. Ashraf, H. AbdAllah and H. M. Abd El-Salam, *Desalination*, 2018, **444**, 129–141.
- 41 M. Sadrzadeh, M. Rezakazemi and T. Mohammadi, *Transp. Prop. Polym. Membr.*, 2018, 391–423.
- 42 A. F. Ismail, *Compr. Membr. Sci. Eng.*, 2010, **1**, 275–290.
- 43 W. Salim and W. S. W. Ho, *Curr. Opin. Chem. Eng.*, DOI: [10.1016/j.coche.2015.03.003](https://doi.org/10.1016/j.coche.2015.03.003).



- 44 D. Emadzadeh, W. J. Lau, T. Matsuura, M. Rahbari-Sisakht and A. F. Ismail, *Chem. Eng. J.*, 2014, **237**, 70–80.
- 45 N. Akther, S. Phuntsho, Y. Chen, N. Gha and H. Kyong, *J. Membr. Sci.*, 2019, **584**, 20–45.
- 46 Y. Wang, R. Ou, H. Wang and T. Xu, *J. Membr. Sci.*, 2015, **475**, 281–289.
- 47 X. Chang, Z. Wang, S. Quan, Y. Xu, Z. Jiang and L. Shao, *Appl. Surf. Sci.*, 2014, **316**, 537–548.
- 48 R. A. Milesu, C. R. McElroy, T. J. Farmer, P. M. Williams, M. J. Walters and J. H. Clark, *Adv. Polym. Technol.*, 2019, **2019**, 9692859.
- 49 S. Wu, Y. Cheng, J. Ma, Q. Huang, Y. Dong, J. Duan, D. Mo, Y. Sun, J. Liu and H. Yao, *J. Membr. Sci.*, 2021, **635**, 119467.
- 50 C. Zhao, J. Xue, F. Ran and S. Sun, *Prog. Mater. Sci.*, 2013, **58**, 76–150.
- 51 J. F. Blanco, J. Sublet, Q. T. Nguyen and P. Schaetzel, *J. Membr. Sci.*, 2006, **283**, 27–37.
- 52 M. Shaban, A. M. Ashraf, H. Abdallah and H. M. A. El-salam, *Desalination*, 2018, **1**.
- 53 M. Amini, M. Jahanshahi and A. Rahimpour, *J. Membr. Sci.*, 2013, **435**, 233–241.
- 54 S. Sahebi, S. Phuntsho, L. Tijing, G. Han, D. S. Han, A. Abdel-Wahab and H. K. Shon, *Desalination*, 2017, **406**, 98–108.
- 55 R. R. Gonzales, M. J. Park, T. H. Bae, Y. Yang, A. Abdel-Wahab, S. Phuntsho and H. K. Shon, *Desalination*, 2019, **459**, 10–19.
- 56 L. Zhao, Y. Huang, B. Liu, Y. Huang, A. Song, Y. Lin, M. Wang, X. Li and H. Cao, *Electrochim. Acta*, 2018, **278**, 1–12.
- 57 A. K. Holda and I. F. J. Vankelecom, *J. Appl. Polym. Sci.*, 2015, **132**, 42130.
- 58 B. Piluharto, V. Suendo, T. Ciptati and C. L. Radiman, *Ionics*, 2011, **17**, 229–238.
- 59 N. Gholami and H. Mahdavi, *Adv. Polym. Technol.*, 2018, **37**, 3529–3541.
- 60 V. D. Alves and I. M. Coelhoso, *J. Membr. Sci.*, 2004, **228**, 159–167.
- 61 R. Wang, L. Shi, C. Y. Tang, S. Chou, C. Qiu and A. G. Fane, *J. Membr. Sci.*, 2010, **355**, 158–167.
- 62 H. M. Ali, H. Gadallah, S. S. Ali, R. Sabry and A. G. Gadallah, *Int. J. Chem. Eng.*, 2016, **2016**, 8745943.
- 63 D. Emadzadeh, W. J. Lau and A. F. Ismail, *Desalination*, 2013, **330**, 90–99.
- 64 S. A. Soomro, I. H. Gul, H. Naseer, S. Marwat and M. Mujahid, *Curr. Nanosci.*, 2018, **15**, 420–429.
- 65 M. Zayed, A. M. Ahmed and M. Shaban, *Int. J. Hydrogen Energy*, 2019, **44**, 17630–17648.
- 66 M. Shaban, M. Zayed and H. Hamdy, *RSC Adv.*, 2017, **7**, 617–631.
- 67 R. Siburian, H. Sihotang, S. Lumban Raja, M. Supeno and C. Simanjuntak, *Orient. J. Chem.*, 2018, **34**, 182–187.
- 68 L. Yu, Y. Zhang, B. Zhang, J. Liu, H. Zhang and C. Song, *J. Membr. Sci.*, 2013, **447**, 452–462.
- 69 J. Bin Wu, M. L. Lin, X. Cong, H. N. Liu and P. H. Tan, *Chem. Soc. Rev.*, 2018, **47**, 1822–1873.
- 70 A. T. Smith, A. M. LaChance, S. Zeng, B. Liu and L. Sun, *Nano Mater. Sci.*, 2019, **1**, 31–47.
- 71 L. Yu, Y. Zhang, B. Zhang, J. Liu, H. Zhang and C. Song, *J. Membr. Sci.*, 2013, **447**, 452–462.
- 72 B. M. Ganesh, A. M. Isloor and A. F. Ismail, *Desalination*, 2013, **313**, 199–207.
- 73 J. H. Choi, J. Jegal and W. N. Kim, *J. Membr. Sci.*, 2006, **284**, 406–415.
- 74 I. M. Wienk, R. M. Boom, M. A. M. Beerlage, A. M. W. Bulte, C. A. Smolders and H. Strathmann, *J. Membr. Sci.*, 1996, **113**, 361–371.
- 75 S. Lim, M. J. Park, S. Phuntsho, L. D. Tijing, G. M. Nisola, W.-G. Shim, W.-J. Chung and H. K. Shon, *Polymer*, 2017, **110**, 36–48.
- 76 D. F. Ahmed, H. Isawi, N. A. Badway, A. A. Elbayaa and H. Shawky, *Arabian J. Chem.*, 2021, **14**, 102995.
- 77 A. A. Shamsuri, S. N. A. M. Jamil and K. Abdan, *Process*, 2021, **9**, 480.
- 78 A. M. Alosaimi, *Polymers*, 2021, **13**(16), 2792.
- 79 A. Alkhouzaam and H. Qiblawey, *J. Water Proc. Eng.*, 2021, **42**, 102120.
- 80 R. J. Kadhim, F. H. Al-Ani, M. Al-Shaeli, Q. F. Alsalhy and A. Figoli, *Membr.*, 2020, **10**, 366.
- 81 Z. Li, Y. Wang, M. Han, D. Wang, S. Han, Z. Liu, N. Zhou, R. Shang and C. Xie, *Front. Chem.*, 2020, **7**, 1–12.
- 82 I. Khan, K. Saeed and I. Khan, *Arabian J. Chem.*, 2019, **12**, 908–931.
- 83 Z. Li, Y. Wang, M. Han, D. Wang, S. Han, Z. Liu, N. Zhou, R. Shang and C. Xie, *Front. Chem.*, 2020, **7**, 1–12.
- 84 H. G. Lemos, R. A. Ragio, A. C. S. Conceição, E. C. Venancio, J. C. Mierzwa and E. L. Subtil, *Chem. Eng. J.*, 2021, **425**, 131772.
- 85 M. Amini, M. Jahanshahi and A. Rahimpour, *J. Membr. Sci.*, 2013, **435**, 233–241.
- 86 C. S. Lin, K. L. Tung, Y. L. Lin, C. Di Dong, C. W. Chen and C. H. Wu, *Process Saf. Environ. Prot.*, 2020, **144**, 225–235.
- 87 D. Emadzadeh, W. J. Lau, T. Matsuura, A. F. Ismail and M. Rahbari-Sisakht, *J. Membr. Sci.*, 2014, **449**, 74–85.
- 88 Q. Liu, L. Li, X. Jin, C. Wang and T. Wang, *J. Mater. Sci.*, 2018, **53**, 6505–6518.
- 89 G. R. Xu, X. Y. Liu, J. M. Xu, L. Li, H. C. Su, H. L. Zhao and H. J. Feng, *Appl. Surf. Sci.*, 2018, **434**, 573–581.
- 90 A. Marjani, A. T. Nakhjiri, M. Adimi, H. F. Jirandehi and S. Shirazian, *Sci. Rep.*, 2020, **10**, 1–11.
- 91 W. Zhao, J. Huang, B. Fang, S. Nie, N. Yi, B. Su, H. Li and C. Zhao, *J. Membr. Sci.*, 2011, **369**, 258–266.
- 92 R. Rezaee, S. Nasseri, A. H. Mahvi, R. Nabizadeh, S. A. Mousavi, A. Rashidi, A. Jafari and S. Nazmara, *J. Environ. Health Sci. Eng.*, 2015, **13**, 61.
- 93 W. A. Phillip, J. S. Yong and M. Elimelech, *Environ. Sci. Technol.*, 2010, **44**, 5170–5176.
- 94 E. Arkhangelsky, F. Wicaksana, S. Chou, A. A. Al-Rabiah, S. M. Al-Zahrani and R. Wang, *J. Membr. Sci.*, 2012, **415–416**, 101–108.
- 95 Q. Yang, J. Lei, D. D. Sun and D. Chen, *Sep. Purif. Rev.*, 2016, **45**, 93–107.



- 96 N. L. Le and S. P. Nunes, *Sustainable Mater. Technol.*, 2016, **7**, 1–28.
- 97 J. Zhu, J. Hou, A. Uliana, Y. Zhang, M. Tiana and B. V. der Bruggen, *J. Mater. Chem. A*, 2018, **6**, 3773–3792.
- 98 M. H. Zadeh, H. Mighani and A. Shakeri, *J. Polym. Res.*, 2022, **29**, 169.
- 99 J.-N. Shen, H.-M. Ruan, L.-G. Wu and C.-J. Gao, *Chem. Eng. J.*, 2011, **168**, 1272–1278.
- 100 X. Shi, G. Tal, N. P. Hankins and V. Gitis, *J. Water Proc. Eng.*, 2014, **1**, 121–138.
- 101 J. R. McCutcheon and M. Elimelech, *J. Membr. Sci.*, 2008, **318**, 458–466.

